

Orbital-selective charge-density wave in TaTe₄

R. Z. Xu¹, X. Du¹, J. S. Zhou¹, X. Gu¹, Q. Q. Zhang¹, Y. D. Li¹, W. X. Zhao¹, F. W. Zheng², M. Arita³, K. Shimada³, T.

K. Kim⁴, C. Cacho⁴, Y. F. Guo^{5,6}, Z. K. Liu^{5,6}, Y. L. Chen^{1,5,6,7}, L. X. Yang^{1,8,9}

¹*State Key Laboratory of Low Dimensional Quantum Physics, Department of Physics, Tsinghua University, Beijing 100084, China*

²*Institute of Applied Physics and Computational Mathematics, Beijing 100088, China*

³*Hiroshima Synchrotron Radiation Center, Hiroshima University, Higashi-Hiroshima 739-0046, Japan*

⁴*Diamond Light Source, Harwell Science & Innovation Campus, Didcot, Oxfordshire – OX11 0QX, U.K.*

⁵*School of Physical Science and Technology, ShanghaiTech University and CAS-Shanghai Science Research Center, Shanghai 201210, China.*

⁶*ShanghaiTech Laboratory for Topological Physics, Shanghai 200031, China.*

⁷*Clarendon Laboratory, Department of Physics, University of Oxford, Oxford OX1 3PU, U.K.*

⁸*Frontier Science Center for Quantum Information, Beijing 100084, China*

⁹*Collaborative Innovation Center of Quantum Matter, Beijing 100871, China*

TaTe₄, a metallic charge-density wave (CDW) material discovered decades ago, has attracted renewed attention due to its rich interesting properties such as pressure-induced superconductivity and candidate non-trivial topological phase. Here, using high-resolution angle-resolved photoemission spectroscopy and *ab-initio* calculation, we systematically investigate the electronic structure of TaTe₄. At 26 K, we observe a CDW gap as large as 290 meV, which persists up to 500 K. The CDW-modulated band structure shows a complex reconstruction that closely correlates with the lattice distortion. Inside the CDW gap, there exist highly dispersive energy bands contributing to the remnant Fermi surface and metallic behavior in the CDW state. Interestingly, our *ab-initio* calculation reveals that the large CDW gap mainly opens in the electronic states with out-of-plane orbital components, while the in-gap metallic states originate from in-plane orbitals, suggesting an orbital texture that couples with the CDW order. Our results shed light on the interplay between electron, lattice, and orbital in quasi-one-dimensional CDW materials.

INTRODUCTION

Charge density waves (CDWs), long-range order of electron density on the positive background of periodic lattice distortion (PLD), have been discovered and extensively studied for decades¹⁻³. While CDWs have been widely observed and suggested to be closely related to many intriguing emergent phenomena, such as high-temperature superconductors in cuprates⁴, heavy fermion behavior⁵, and topological quantum states⁶⁻⁸, the mechanism of CDW transition is still under debate and seems to be materials-dependent⁹⁻¹³. As originally proposed by Peierls, the perfect Fermi surface (FS) nesting in one-dimensional metallic systems induces a divergence in the electronic response function and enhances the electronic screening of the phonons with the momentum of twice the electron Fermi momentum, which facilitates the formation of the PLD and CDW. In real materials, however, this picture has been challenged since the FS nesting is usually imperfect and incapable to drive the lattice distortion¹². In some systems, such as the Luttinger liquid materials,

CDW can also emerge with strongly suppressed electronic states near the Fermi level (E_F)^{9,14-16}. Alternatively, a scenario of momentum-dependent electron-phonon coupling was proposed to play a vital role in the formation of CDWs^{12,17}.

In addition, the orbital degree of freedom is also involved in the CDW ordering in many two-dimensional CDW materials¹⁸⁻²⁵. On the one hand, complex orbital texture has been shown to intertwine with the CDWs in different materials^{22,26}. On the other hand, the orbital hybridization and ordering can strongly modulate the electronic states near E_F , thus affecting or driving the CDW formation. For example, in the monolayer TiTe_2 , the selective hybridization between orbitals can greatly save the total energy of the system and favor the CDW transition²¹. Recently, orbital hybridization is likewise shown to be able to drive the CDW transition in the kagome material CsV_3Sb_5 ^{27,28}. It is therefore of paramount importance to investigate the interplay between electron, orbital, and lattice in the CDW ordered states for a comprehensive picture of CDW transitions.

Transition metal tetrachalcogenide TaTe_4 is a prototypical quasi-one-dimensional (Q1D) CDW material discovered in the 1960s²⁹⁻³⁵. Recently, it attracts renewed research interests due to its rich intriguing properties such as superconductivity under high pressure³⁶, nontrivial topological properties^{34,37,38}, and large anisotropic magnetoresistance^{37,38}. After extensive studies, however, there are still mysteries in the CDW properties of TaTe_4 . Firstly, TaTe_4 shows metallic behavior in the CDW state, despite a large CDW gap of about 300 meV observed by optical conductivity and angle-resolved photoemission spectroscopy (ARPES) measurements³¹. Secondly, although TaTe_4 exhibits a Q1D crystal structure, no Q1D band dispersion was directly observed in previous ARPES measurements³¹. Thirdly, the mechanism of the CDW transition in TaTe_4 is still elusive: while the FS nesting is excluded by recent calculations of the electronic structure, it is still under debate whether the softened phonon modes originate from strong electron-phonon coupling or structural optimization^{35,39}. Moreover, the surface CDW modulation is sensitive to the external magnetic field, suggesting a complex interplay between different degrees of freedom in the CDW ordering³².

In this work, we study the electronic structure of TaTe₄ using high-resolution ARPES. At low temperatures, we observe a CDW gap of about 290 meV, much larger than the mean-field estimation of $3.5 k_B T_c$, where T_c is the CDW transition temperature of TaTe₄. Inside the CDW gap, we observe dispersive bands forming Q1D FS sheets and accounting for the metallic behavior in the CDW state. Our *ab-initio* calculation confirms the irrelevance of FS nesting in the CDW transition, consistent with previous results. Moreover, the large CDW gap selectively opens in the electronic states of out-of-*ab*-plane orbital components, while the in-gap band dispersions of in-*ab*-plane orbital components show weak reconstruction, suggesting an intriguing orbital-selective CDW formation in TaTe₄. Our results provide important insights into the interplay between electron, lattice, and orbital degrees of freedom in the CDW state of Q1D TaTe₄.

RESULTS

Basic properties of TaTe₄

TaTe₄ crystallizes in a tetragonal structure with $P4/mcc$ space group in the normal state³⁹. Each Ta atom is coordinated with eight Te atoms, forming Q1D chains of face-sharing square antiprisms along the c direction, as schematically shown in Fig. 1a. With decreasing temperature, the system first enters a $\sqrt{2}a \times \sqrt{2}a \times 3c$ commensurate CDW (CCDW) state, then a $2a \times 2a \times 3c$ CCDW' state below $T'_{\text{CCDW}} \approx 450$ K (Fig. 1b)^{30,40,41}. The CCDW' transition is manifested in the magnetic susceptibility measurement in Fig. 1c, where we observe an anomaly in the slope of the χ - T curve near 450 K. Figure 1d shows the Raman scattering data at selected temperatures. With increasing temperature, most of the Raman peaks shift toward lower energies. We noted that the peak at about 58 cm⁻¹ (marked by the black arrow) shows a minor shift but a significant reduction of its intensity (about 80%), which may be related to the CCDW' transition (Supplementary Note 1).

Figure 1e and 1f show the *ab-initio* calculations of the band structure of TaTe₄ in the normal state without and with the spin-orbit coupling (SOC) effect. SOC exerts a strong influence on the electronic structure by opening large gaps at the band crossings along Γ -X-M- Γ as shown in Fig.

1f. The Fermi momenta of the energy bands, however, is far from the CDW wavevector, as exemplified by the black arrow along ΓZ in the inset of Fig. 1f. Even after the calculated chemical potential is aligned to the experimental value (Supplementary Note 4), the theoretical Fermi momenta is still different from the CDW wave vector, confirming the irrelevance of the FS nesting in the CDW transition¹².

Figure 2 shows the calculated and ARPES-measured FS of TaTe₄. In the normal state, we reveal three FS sheets: a warped Q1D open FS (blue sheets in Fig. 2a) and two 3D closed pockets around the M and A points (green sheets in Fig. 2a). To better compare with the experiments, Fig. 2b shows the overlaid FS in the ΓZRX and $XRAM$ planes. In the $2 \times 2 \times 3$ CCDW' state, the FS shows a drastic reconstruction. We observe four FS sheets in the Brillouin zone of the CCDW' state (Fig. 2c). The green open FS sheet is nearly dispersionless along k_z , which may be important for the intriguing magnetotransport properties of TaTe₄^{37,38}. Fig. 2d shows the 2D plot of the FS in the CCDW' state in the γzrx plane.

Since the sample is cleaved along the (010) plane as shown in Fig. 1a, ARPES measurement is conducted in the k_x - k_z plane. Figure 2e presents the measured FS with a large electron pocket at the \bar{X} point and quasi-1D FS sheets along k_x . Both the Fermi surface sheets are captured by the calculation despite the differences in the fine details. It is worth noting that the band structure along ΓX can also be measured by photon-energy-dependent experiments due to the tetragonal crystal structure. Figure 2f presents the FS measured along k_y . We observe a clear reconstruction of the Q1D FS sheets along k_z (due to the weak intensity at E_F , we show the data at 150 meV below E_F) within the expectation of the 3-fold band folding along k_z (Supplementary Note 5). The folding of the in-gap states induces eye-shape features in the k_x - k_z map, which can be better visualized in the constant-energy-contours at higher binding energies (Supplementary Note 3)⁴².

Band reconstruction with the CDW formation

Figure 3a shows the measured band dispersions along $\bar{\Gamma}\bar{Z}$. Consistent with the previous measurement³¹, we observe a large gap of about 290 meV and multiple dispersive bands in the high binding energies (also see Supplementary Notes 6 and 7). Besides, there exist noticeable features with weak intensity in the large CDW gap. In the zoom-in plot of ARPES spectra in the CDW gap region (Fig. 3b), we reveal highly dispersive bands crossing E_F , which contribute to the FS in the CCDW' state and account for the metallic transport behavior of the system at low temperatures³¹. To investigate the interplay between the electronic reconstruction and lattice distortion, we calculate the electronic structure of TaTe₄ along ΓZ with different PLD magnitudes as shown in Fig. 3c-3f. With the development of the lattice distortion, the folded bands hybridize with the original bands and the CDW gap gradually increases. At 100% PLD distortion level (corresponding to experimental lattice distortion), the CDW gap is as large as 300 meV, in good agreement with our experiment. Moreover, the in-gap states are well captured by the calculation (Fig. 3f). By comparing the measured and calculated band structures, we reveal clear evidence for the band reconstruction due to CDW superstructure along the c direction (Supplementary Note 2).

Orbital-selective CDW gap formation

We notice that the magnitude of the CDW gap varies in different bands. For example, in Fig. 3c, the α band (highlighted by yellow thick lines in Fig. 3d-f) is much more sensitive to the lattice distortion than the β band (highlighted by green thick lines). To understand this difference, we calculate the orbital-projected band structure of TaTe₄ in Fig. 4. As shown in Fig. 4a and 4b, along the ΓZ direction, the α (β) band in the normal state mainly consists of out-of- ab -plane (in- ab -plane) Ta $5d_{z^2}$ ($5d_{x^2-y^2}$) orbital hybridized with Te $5p_z$ ($5p_{x/y}$) orbital. In the CCDW' state, the d_{z^2} orbital components are strongly affected by opening a large CDW gap, while the $d_{x^2-y^2}$ orbital components show weak change. Along other momentum directions, the $d_{x^2-y^2}$ orbitals are likewise highly dispersive and contribute to band dispersions crossing E_F (Fig. 4c and 4d), while

the global orbital-selective CDW gap induces narrow bands (bandwidth ~ 200 meV) with d_{z^2} orbitals. Such an orbital-dependent reconstruction of the electronic structure with CDW ordering resembles the orbital texture in the CCDW state of 1T-TaSe₂²², suggesting an intriguing interplay between charge, lattice, and orbital degrees of freedom in TaTe₄.

DISCUSSIONS

Our experiment and calculation suggest that the FS nesting is irrelevant in the CDW transition of TaTe₄. Firstly, the Fermi momenta of the calculated and experimental band structure deviate from the CDW wavevector along k_z . Secondly, we observe a reduced CDW gap of $\frac{2\Delta}{k_B T'_{\text{CCDW}}} \approx 15$, which is much larger than the mean-field estimation, evincing a strong-coupling nature of the CDW (even with the highest reported CCDW transition temperature of 650 K⁴³, the reduced gap is still much larger than 3.5). Correspondingly, the distortion of Ta atoms is about 6.6% of the lattice constant⁴⁴, similar to that in 1T-TaS₂, a well-known strong-coupling CDW material⁴⁵. Thirdly, previous calculations of the phonon spectrum revealed a broad phonon softening, which was understood by the strong electron-phonon interaction instead of Fermi surface nesting³⁹. The phonon frequencies decrease in a broad momentum range and drop to minus values around \vec{q}_{CDW} ³⁹ similar to the situation in NbSe₂⁴⁶ and monolayer VTe₂¹⁷ where the CDW transition is explained by a momentum-dependent EPC model^{17,46,47}.

On the other hand, while CDW is an electron-phonon intertwined state, other degrees of freedom such as orbital and spin can be deeply involved by modulating the electronic states near E_F ^{23,48-50}. In TaTe₄, due to the Q1D crystal structure, the lattice distortion is highly anisotropic. In the CDW state at low temperatures, the Ta-Te bonds expand by about 2.8% and the Ta-Ta distance remains unchanged. By contrast, the displacement of Ta atoms is as large as 6.6% of c along the z -axis⁴⁴. This anisotropic lattice distortion provides a structural basis for the strong interaction between the d_{z^2} orbital-derived electronic states. The interplay between electron, lattice, and

orbital results in the intriguing orbital-selective CDW state with metallic in-gap states, which provides an interesting platform to explore the orbital-selective transport properties or orbitronics.

In summary, our results show that the metallic properties of CDW ordering in TaTe₄ originate from dispersive in-gap states. We reveal an orbital-selective formation of the CDW gap, suggesting a complex interplay between electron, lattice, and orbital degrees of freedom in the CDW transition of TaTe₄.

METHODS

Sample preparation

High-quality TaTe₄ single crystals were synthesized by the self-flux method using tellurium flux. Tantalum (99.9%, Aladdin Chemicals) and tellurium (99.999%, Aladdin Chemicals) powders were mixed in the molar ratio of Ta: Te = 1: 30 and placed into an alumina crucible. Under a vacuum lower than 10^{-4} Pa, the crucible is sealed into a quartz tube and heated slowly up to 1000 °C within 15 hours. The temperature was kept at 1000 °C for around 20 hours so that the two substances fully react. After cooling the system uniformly down to 550 °C, the quartz tube was quickly transferred to a centrifuge to separate the excess tellurium. We examine the crystalline phase and sample qualities by Bruker D8 VENTURE single crystal diffractometer utilizing Mo K_α1 radiation with a wavelength of 0.7093 Å.

ARPES measurements

High-resolution ARPES experiments were performed at beamline 9A of Hiroshima Synchrotron Radiation Center (HSRC) and beamline I05 of Diamond Light Source (DLS)⁵¹ using Scienta R4000 analyzers. ARPES measurements above 400 K were conducted at Peking University using a Scienta DA30L analyzer and a helium discharge lamp. The convolved energy and angular resolutions were 15 meV and 0.2° respectively. The samples were cleaved *in situ* and measured under ultrahigh vacuum below 1×10^{-10} mbar.

Band structure calculations

The distortion-dependent band structures were calculated using Vienna Ab initio Software Package (vasp)⁵². The atom core electrons were described by the projector augmented wave (PAW) method^{53,54}. The Perdew-Burke-Ernzerhof (PBE) functional⁵⁵ was used to treat the electronic exchange correlation. The plane-wave energy cut-off was set to 350 eV. The reciprocal space was sampled with a Monkhorst-Pack grid $8 \times 8 \times 8$ for the normal-state unit-cell and a grid $3 \times 3 \times 2$ for $2a \times 2a \times 3c$ supercell. The cut-off energy and Monkhorst-pack grids were converged to produce reliable electronic structures. The atomic structure was relaxed until the force on each atom is smaller than 0.01 eV/Å. We have used the van der Waals correction⁵⁶ and spin-orbit coupling correction for the density-functional-theory calculations.

The orbital-projected band structures were calculated using QUANTUM ESPRESSO package⁵⁷ with a plane wave basis. The exchange-correlation energies were considered under Perdew-Burke-Ernzerhof (PBE) type generalized gradient approximation (GGA)⁵⁵. Both cases of excluding and including spin-orbit coupling were considered. The cutoff energy for the plane-wave basis was set to 400 eV. A Γ -centered Monkhorst-Pack k -point mesh of $7 \times 7 \times 7$ was adopted for a self-consistent charge density.

DATA AVAILABILITY

The data supporting the conclusions in this work are available from the corresponding authors.

ACKNOWLEDGMENTS

This work was supported by the National Natural Science Foundation of China (Grant No. 12274251) and the National Key R&D program of China (Grants No. 2022YFA1403201 and 2022YFA1403100). L.X.Y. acknowledges the support from the Tsinghua University Initiative Scientific Research Program and the Fund of Science and Technology on Surface Physics and

Chemistry Laboratory (No. XKFZ202102). Y.L.C. acknowledges the support from the Oxford-ShanghaiTech collaboration project and the Shanghai Municipal Science and Technology Major Project (grant 2018SHZDZX02). Y.F.G. acknowledges the the Double First-Class Initiative Fund of ShanghaiTech University. We thank Diamond Light Source for access to beamline I05 (Proposal number SI20683-1) that contributed to the results presented here. ARPES experiments at the Hiroshima Synchrotron Radiation Center (HiSOR), Hiroshima University were done under Proposal No. 18BG051. We thank N-BARD, Hiroshima University, for supplying the liquid helium.

COMPETING INTERESTS

The authors declare no Competing Financial or Non-Financial Interests.

AUTHOR CONTRIBUTIONS

L.X.Y. and Y.L.C. conceived and supervised the experiments. R.Z.X. and X.D. contributed equally to this paper. R.Z.X. carried out the ARPES experiments and corresponding analysis with the assistance of X.D., J.S.Z., X.G., Q.Q.Z., Y.D.L., W.X.Z., M.A., K.S., T.K.K., C.C., Z.K.L. X.D. performed the *ab-initio* calculations with the assistance of F.W.Z. Y.F.G provided high-quality single crystal samples. R.Z.X. wrote the first draft of the paper. L.X.Y., Z.K.L. and Y.L.C. contributed to the revision of the manuscript. R.Z.X and X.D. contributed to this work equally. All authors contributed to the scientific planning and discussions.

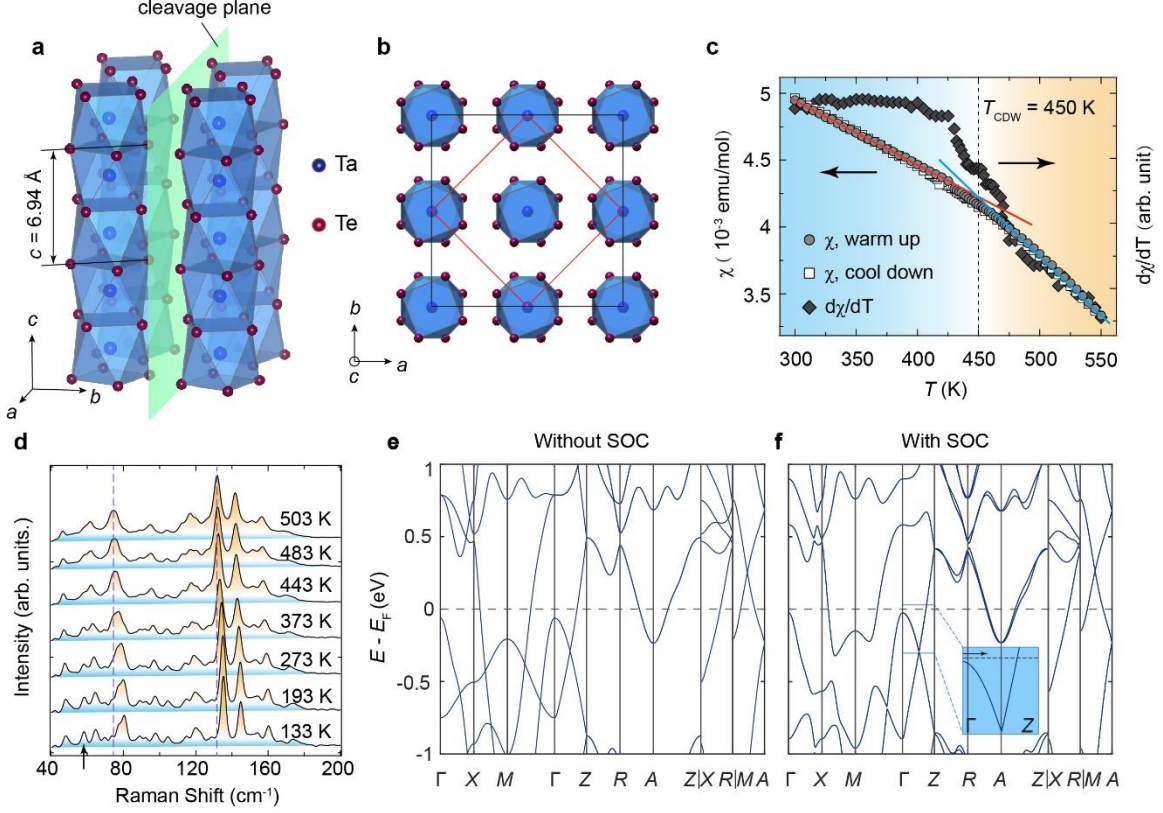


Fig. 1. Basic properties of TaTe₄. **a-b** Crystal structure of TaTe₄ in the front view (**a**) and top view (**b**). The green plane indicates the cleavage plane. Black and red lines indicate the superlattices of the $2a \times 2a \times 3c$ CCDW' and $\sqrt{2}a \times \sqrt{2}a \times 3c$ CCDW states. **c** Magnetic susceptibility of TaTe₄ as a function of temperature. The red and blue lines are guides to eyes for the change of the slope near $T'_{\text{CCDW}} = 450$ K. **d** Raman scattering spectra at selected temperatures from 130 K to 503 K. **e-f** Calculated band structure of TaTe₄ in the normal state without (**e**) and with (**f**) spin-orbit coupling (SOC). The inset shows the band structure along ΓZ near the Fermi level (E_F) with the black arrow indicating the CCDW' wavevector.

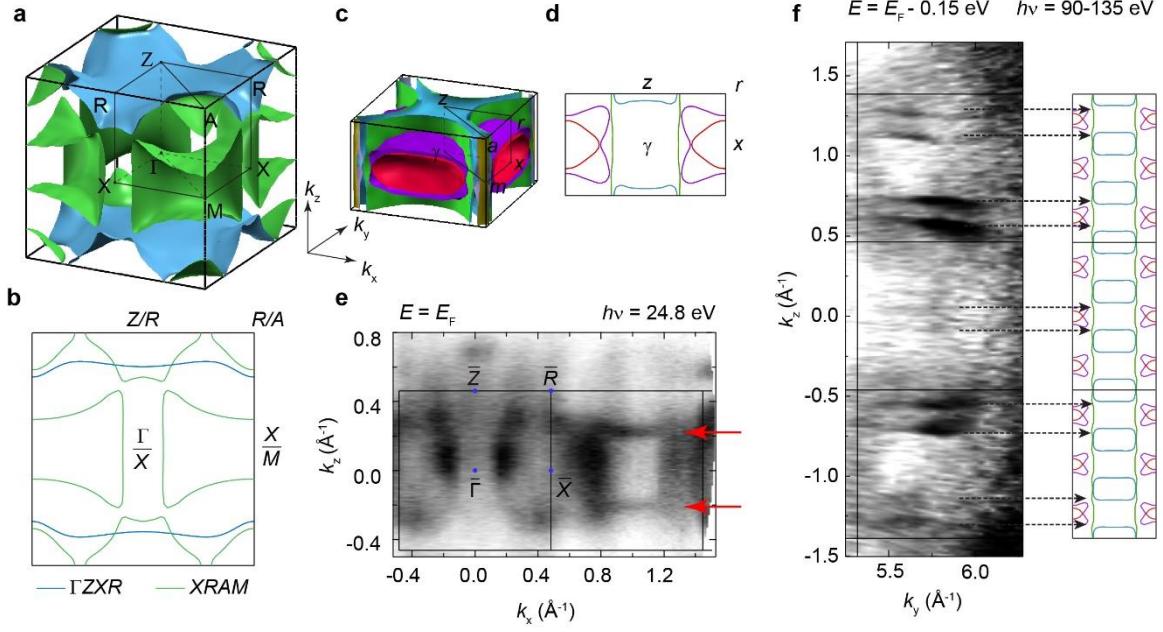


Fig. 2. Calculated and experimental Fermi surface (FS) of TaTe₄. **a** Calculated FS in the normal state in the bulk Brillouin zone (BZ) (**a**). **b** Overlaid FS contours in the ΓZRX (blue curves) and $XRAM$ (green curves) planes. **c** Calculated FS in the CCDW' state. **d** FS contour in the γzrx plane. The uppercase and lowercase letters mark the high symmetry points of the BZ in the normal states and CCDW' states respectively. **e** FS measured using linear-horizontally polarized photons at 24.8 eV at 40 K. **f** Constant-energy-contour at 0.15 eV below E_F measured by photon-energy-dependent experiments using linear-horizontally (LH) polarized photons at 40 K. The photon energy ranges from 90 to 135 eV. The calculated result at 0.21 eV below E_F considering the chemical potential difference between the experiment and calculation (Supplementary Note 4) is shown side-by-side for comparison.

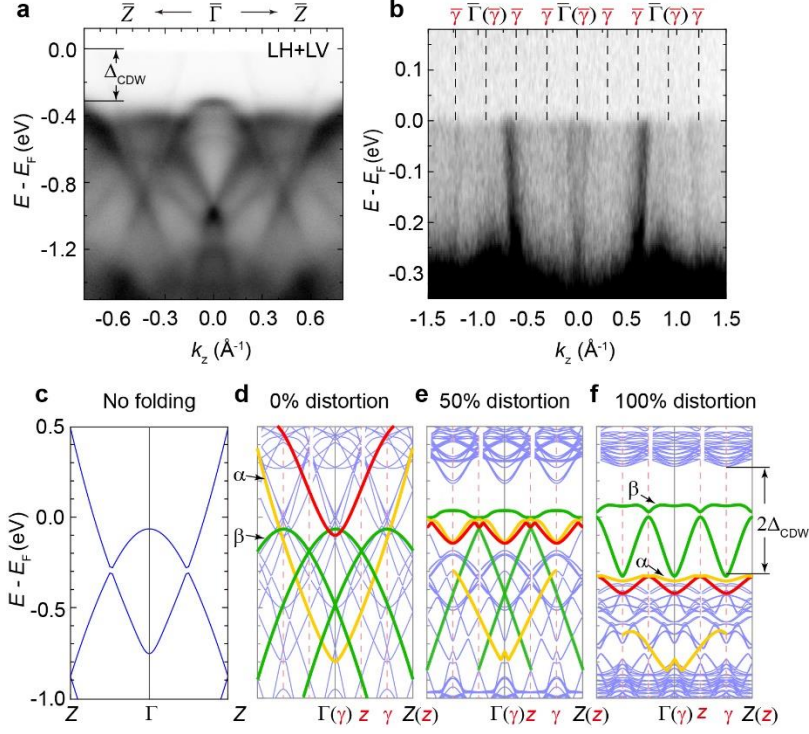


Fig. 3. Evolution of the band structure of TaTe₄ with periodic lattice distortion (PLD). **a** Band dispersions along the $\bar{\Gamma}\bar{Z}$ direction measured at 40 K. The ARPES spectra measured by LH and linear-vertically (LV) polarized photons are summed together. **b** Zoom-in plot of the band structure in the CDW gap. **c** Calculated electronic structure of TaTe₄ in the normal state. **d-f** Evolution of the calculated band structure along the ΓZ direction with increasing PLD magnitudes. The yellow and green lines in **d** are the bands along ΓZ . The red line in **d** is the band along XR which was folded to the ΓZ direction. Data in **a** and **b** were collected using 24.8 eV and 100 eV photons respectively.

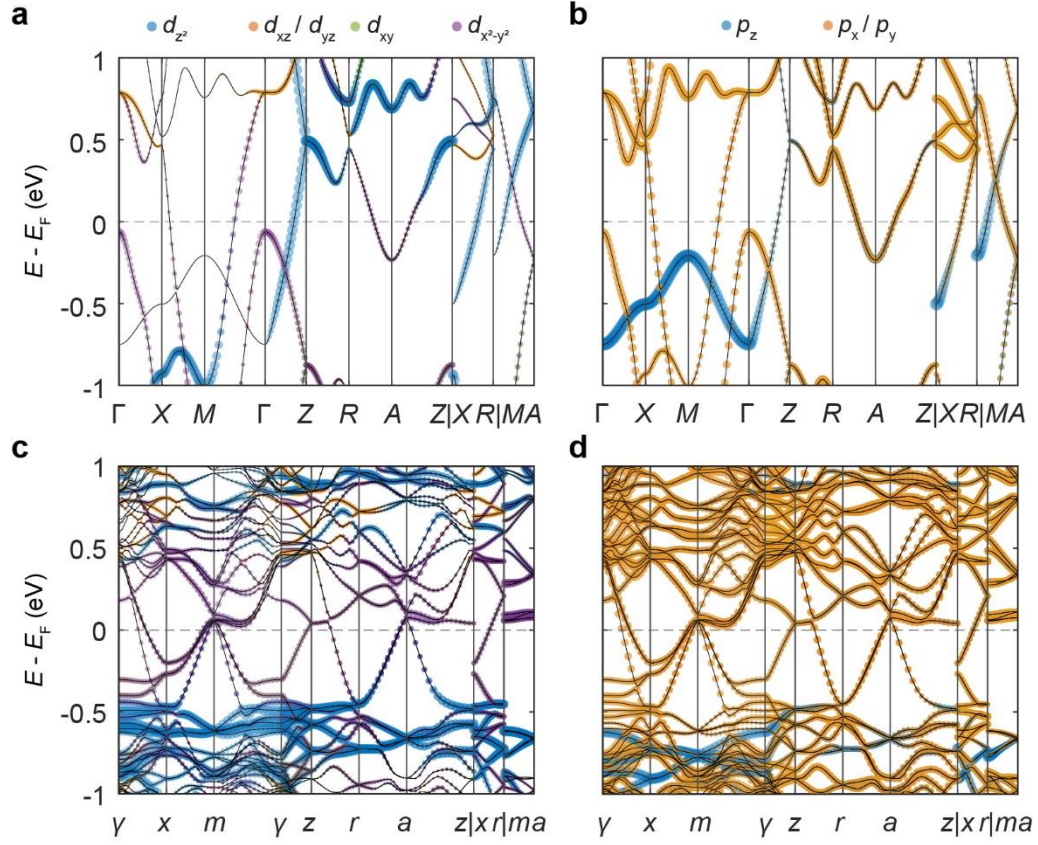


Fig. 4. Orbital-projected calculations of the band structure of TaTe₄. **a-b** Contribution from Ta *d*-orbitals (**a**) and Te *p*-orbitals (**b**) in the normal state. **c-d** Same as **a-b** but in the CCDW' state. The *xyz* framework corresponds to the lattice coordinate *abc* respectively.

Reference

1. Grüner, G. & Zettl, A. Charge density wave conduction: A novel collective transport phenomenon in solids. *Phys. Rep.* **119**, 117-232 (1985).
2. Grüner, G. The dynamics of charge-density waves. *Rev. Mod. Phys.* **60**, 1129 (1988).
3. Gor'kov, L. P. & Grüner, G. *Charge density waves in solids*. (Elsevier, 2012).
4. Chang, J. *et al.* Direct observation of competition between superconductivity and charge density wave order in $\text{YBa}_2\text{Cu}_3\text{O}_{6.67}$. *Nat. Phys.* **8**, 871-876 (2012).
5. Neilson, J. R. *et al.* Mixed-valence-driven heavy-fermion behavior and superconductivity in KNi_2Se_2 . *Phys. Rev. B* **86**, 054512 (2012).
6. Shi, W. *et al.* Publisher Correction: A charge-density-wave topological semimetal. *Nat. Phys.* **17**, 284 (2021).
7. Cho, S. *et al.* Emergence of New van Hove Singularities in the Charge Density Wave State of a Topological Kagome Metal RbV_3Sb_5 . *Phys. Rev. Lett.* **127**, 236401 (2021).
8. Qin, F. *et al.* Theory for the charge-density-wave mechanism of 3D quantum Hall effect. *Phys. Rev. Lett.* **125**, 206601 (2020).
9. Kang, L. *et al.* Band-selective Holstein polaron in Luttinger liquid material $\text{A}_{0.3}\text{MoO}_3$ ($\text{A} = \text{K}, \text{Rb}$). *Nat. Commun.* **12**, 6183 (2021).
10. Schäfer, J. *et al.* Unusual spectral behavior of charge-density waves with imperfect nesting in a quasi-one-dimensional metal. *Phys. Rev. Lett.* **91**, 066401 (2003).
11. Perfetti, L. *et al.* Mobile small polarons and the Peierls transition in the quasi-one-dimensional conductor $\text{K}_{0.3}\text{MoO}_3$. *Phys. Rev. B* **66**, 075107 (2002).
12. Johannes, M. & Mazin, I. Fermi surface nesting and the origin of charge density waves in metals. *Phys. Rev. B* **77**, 165135 (2008).
13. Shen, D. *et al.* Novel mechanism of a charge density wave in a transition metal dichalcogenide. *Phys. Rev. Lett.* **99**, 216404 (2007).
14. Du, X. *et al.* Crossed Luttinger liquid hidden in a quasi-two-dimensional material. *Nat. Phys.* **19**, 40-45 (2023).
15. Ejima, S., Hager, G. & Fehske, H. Quantum phase transition in a 1D transport model with Boson-affected hopping: luttinger liquid versus charge-density-wave behavior. *Phys. Rev. Lett.* **102**, 106404 (2009).
16. Hohenadler, M., Wellein, G., Bishop, A., Alvermann, A. & Fehske, H. Spectral signatures of the Luttinger liquid to the charge-density-wave transition. *Phys. Rev. B* **73**, 245120 (2006).

17. Wang, Z. *et al.* Decisive role of electron-phonon coupling for phonon and electron instabilities in transition metal dichalcogenides. *Phys. rev. res.* **5**, 013218 (2023).
18. Achkar, A. *et al.* Orbital symmetry of charge-density-wave order in $\text{La}_{1.875}\text{Ba}_{0.125}\text{CuO}_4$ and $\text{YBa}_2\text{Cu}_3\text{O}_{6.67}$. *Nat. Mater.* **15**, 616-620 (2016).
19. Watson, M. D. *et al.* Orbital-and k_z -Selective Hybridization of Se 4p and Ti 3d States in the Charge Density Wave Phase of TiSe_2 . *Phys. Rev. Lett.* **122**, 076404 (2019).
20. McMahon, C. *et al.* Orbital symmetries of charge density wave order in $\text{YBa}_2\text{Cu}_3\text{O}_{6+x}$. *Sci. Adv.* **6**, eaay0345 (2020).
21. Antonelli, T. *et al.* Orbital-selective band hybridisation at the charge density wave transition in monolayer TiTe_2 . *npj Quantum Mater.* **7**, 98 (2022).
22. Ritschel, T. *et al.* Orbital textures and charge density waves in transition metal dichalcogenides. *Nat. Phys.* **11**, 328-331 (2015).
23. Zhao, J. *et al.* Orbital selectivity causing anisotropy and particle-hole asymmetry in the charge density wave gap of 2 H-TaS₂. *Phys. Rev. B* **96**, 125103 (2017).
24. Kim, S. *et al.* Orbital-selective Mott and Peierls transition in H_xVO_2 . *npj Quantum Mater.* **7**, 95 (2022).
25. Gaina, R. *et al.* Long-ranged Cu-based order with d_z^2 orbital character at a $\text{YBa}_2\text{Cu}_3\text{O}_7$ / manganite interface. *npj Quantum Mater.* **6**, 12 (2021).
26. Beaulieu, S. *et al.* Unveiling the orbital texture of 1T- TiTe_2 using intrinsic linear dichroism in multidimensional photoemission spectroscopy. *npj Quantum Mater.* **6**, 93 (2021).
27. Han, S. *et al.* Orbital Hybridization-Driven Charge Density Wave Transition in CsV_3Sb_5 Kagome Superconductor. *Adv. Mater.*, 2209010 (2022).
28. Jeong, M. Y. *et al.* Crucial role of out-of-plane Sb p orbitals in Van Hove singularity formation and electronic correlations in the superconducting kagome metal CsV_3Sb_5 . *Phys. Rev. B* **105**, 235145 (2022).
29. Boswell, F., Prodan, A. & Brandon, J. Charge-density waves in the quasi-one-dimensional compounds NbTe_4 and TaTe_4 . *J. Phys. C: Solid State Phys.* **16**, 1067 (1983).
30. Corbett, J., Hiltz, L., Boswell, F., Bennett, J. & Prodan, A. Determination of the symmetry of charge-density-wave modulations in TaTe_4 by HREM. *Ultramicroscopy* **26**, 43-49 (1988).
31. Zwick, F. *et al.* Coexisting one-dimensional and three-dimensional spectral signatures in TaTe_4 . *Phys. Rev. B* **59**, 7762 (1999).
32. Sun, H. *et al.* Discovery of an unconventional charge modulation on the surface of charge-density-wave material TaTe_4 . *New J. Phys.* **22**, 083025 (2020).

33. Mahy, J., Wiegers, G., Van Landuyt, J. & Amelinckx, S. Evidence for deformation modulated structures in NbTe₄ and TaTe₄. *MRS Online Proceedings Library (OPL)* **21** (1982).
34. Zhang, X. *et al.* Eightfold fermionic excitation in a charge density wave compound. *Phys. Rev. B* **102**, 035125 (2020).
35. Guster, B., Pruneda, M., Ordejón, P. & Canadell, E. Competition between Ta-Ta and Te-Te bonding leading to the commensurate charge density wave in TaTe₄. *Phys. Rev. B* **105**, 064107 (2022).
36. Yuan, Y. *et al.* Pressure-Induced Superconductivity in Topological Semimetal Candidate TaTe₄. *Adv. Electron. Mater.* **6**, 1901260 (2020).
37. Gao, Y. *et al.* Anisotropic large magnetoresistance in TaTe₄ single crystals. *J. Appl. Phys.* **122**, 135101 (2017).
38. Luo, X. *et al.* Resistivity plateau and large magnetoresistance in the charge density wave system TaTe₄. *Appl. Phys. Lett.* **110**, 092401 (2017).
39. Liu, F.-H., Fu, W., Deng, Y.-H., Yuan, Z.-B. & Wu, L.-N. First-principles study of the Kohn anomaly in TaTe₄. *Appl. Phys. Lett.* **119**, 091901 (2021).
40. Boswell, F. W. & Bennett, J. C. *Advances in the crystallographic and microstructural analysis of charge density wave modulated crystals*. Vol. 22 (Springer Science & Business Media, 2012).
41. Walker, M. B. Phenomenological Theory of Charge-Density-Wave Phase Transitions in the NbTe₄—TaTe₄ Series of Compounds. *Nuclear Spectroscopy on Charge Density Wave Systems*, 7-33 (1992).
42. Zhang, Y. *et al.* Charge order in a nonsymmorphic topological crystal TaTe₄. Preprint at <https://arxiv.org/abs/2304.00425> (2023).
43. Kusz, J., Bohm, H. & Bennett, J. Modulated phases in the system Ta_{1-x}Nb_xTe₄. *J. Phys.: Condens. Matter* **7**, 2775 (1995).
44. TaTe₄ Crystal Structure: Datasheet from "PAULING FILE Multinaries Edition – 2022" in SpringerMaterials https://materials.springer.com/isp/crystallographic/docs/sd_0250414 (Springer-Verlag Berlin Heidelberg & Material Phases Data System (MPDS), Switzerland & National Institute for Materials Science (NIMS), Japan, 2022).
45. Brouwer, R. & Jellinek, F. The low-temperature superstructures of 1T-TaSe₂ and 2H-TaSe₂. *Physica, B + C*. **99**, 51-55 (1980).
46. Weber, F. *et al.* Extended Phonon Collapse and the Origin of the Charge-Density Wave in 2 H–NbSe₂. *Phys. Rev. Lett.* **107**, 107403 (2011).
47. Weber, F. *et al.* Optical phonons and the soft mode in 2H-NbSe₂. *Phys. Rev. B* **87**, 245111 (2013).

48. Huecker, M. *et al.* Competing charge, spin, and superconducting orders in underdoped $\text{YBa}_2\text{Cu}_3\text{O}_y$. *Phys. Rev. B* **90**, 054514 (2014).
49. Ge, Y. & Liu, A. Y. Effect of dimensionality and spin-orbit coupling on charge-density-wave transition in 2H-TaSe_2 . *Phys. Rev. B* **86**, 104101 (2012).
50. Teng, X. *et al.* Discovery of charge density wave in a kagome lattice antiferromagnet. *Nature* **609**, 490-495 (2022).
51. Hoesch, M. *et al.* A facility for the analysis of the electronic structures of solids and their surfaces by synchrotron radiation photoelectron spectroscopy. *Rev. Sci. Instrum.* **88**, 013106 (2017).
52. Kresse, G. & Furthmüller, J. Efficient iterative schemes for ab initio total-energy calculations using a plane-wave basis set. *Phys. Rev. B* **54**, 11169 (1996).
53. Kresse, G. & Joubert, D. From ultrasoft pseudopotentials to the projector augmented-wave method. *Phys. Rev. B* **59**, 1758 (1999).
54. Blöchl, P. E. Projector augmented-wave method. *Phys. Rev. B* **50**, 17953 (1994).
55. Perdew, J. P., Burke, K. & Ernzerhof, M. Generalized gradient approximation made simple. *Phys. Rev. Lett.* **77**, 3865 (1996).
56. Klimeš, J., Bowler, D. R. & Michaelides, A. Van der Waals density functionals applied to solids. *Phys. Rev. B* **83**, 195131 (2011).
57. Garrity, K. F., Bennett, J. W., Rabe, K. M. & Vanderbilt, D. Pseudopotentials for high-throughput DFT calculations. *Comput. Mater. Sci.* **81**, 446-452 (2014).